Title

Simulation of local ion transport in lamellar block copolymer electrolytes based on electron micrographs

Journal

Journal of Polymer Science Part B Polymer Physics, 55(3)

ISSN

0887-6266

Authors

Chintapalli, Mahati
Higa, Kenneth
Chen, X Chelsea
et al.

Publication Date

2017-02-01

DOI

10.1002/polb.24268

Simulation of local ion transport in lamellar block copolymer electrolytes based on electron micrographs

Mahati Chintapalli,[1,2] Kenneth Higa,[3] X. Chelsea Chen,[2] Venkat Srinivasan,[3] Nitash P. Balsara[2,3,4]

[1]Department of Materials Science and Engineering, University of California, Berkeley, California 94720, United States

[2]Materials Sciences Division, Lawrence Berkeley National Laboratory, Berkeley, California 94720, United States

[3]Energy Storage and Distributed Resources Division, Lawrence Berkeley National Laboratory, Berkeley, California 94720, United States

[4]Department of Chemical and Biomolecular Engineering, University of California, Berkeley, California 94720, United States

Correspondence to: Nitash P. Balsara (nbalsara@gmail.com), Venkat Srinivasan (vsrinivasan@lbl.gov)

((Additional Supporting Information may be found in the online version of this article.))

ABSTRACT

A method is presented to relate local morphology and ionic conductivity in a solid, lamellar block copolymer electrolyte for lithium batteries, by simulating conductivity through transmission electron micrographs. The electrolyte consists of polystyrene-*block*-poly(ethylene oxide) mixed with lithium bis(trifluoromethanesulfonyl) imide salt (SEO/LiTFSI), where the polystyrene phase is structural phase and the poly(ethylene oxide)/LiTFSI phase is ionically conductive. The electric potential distribution is simulated in binarized micrographs by solving the Laplace equation with constant potential boundary conditions. A morphology factor, f, is reported for each image by calculating the effective conductivity relative to a homogenous conductor. Images from two samples are examined, one annealed with large lamellar grains and one unannealed with small grains. The average value of f is 0.45±0.04 for the annealed sample, 0.37±0.03 for the unannealed sample, both close to the value predicted by effective medium theory, 1/2. Simulated conductivities are compared to published experimental conductivities. The value of $f_{Unannealed}/f_{Annealed}$ is 0.82 for simulations and 6.2 for experiments. Simulation results correspond well to predictions by effective medium theory but do not explain the experimental measurements. Observation of nanoscale morphology over length scales greater than the size of the micrographs (~1 µm) may be required to explain the experimental results.

KEYWORDS: electrolyte, transmission electron microscopy, block copolymer, ionic conductivity

INTRODUCTION

Block copolymers in which one microphase is mechanically rigid and the other microphase transports a chemical species are important in a wide range of applications including proton transport membranes in fuel cells,[1–6] selective membranes for separations,[7–15] and electrolytes for high energy density lithium metal batteries.[16–22] Microphase separation between components of a block copolymer allows incompatible properties such as mechanical

strength and chemical permeability to be decoupled.[23] Microphase separation also gives rise to ordered morphologies with characteristic dimensions in the 5 to 50 nm range. Coherent order is limited to another characteristic length scale that is often referred to as the grain size, *L*. The influence of nanoscale morphology and defects on the transport of chemical through block copolymer domains is not yet well understood. While techniques used for morphology characterization such as scattering and microscopy are inherently local (i.e. sensitive to structure on the nanometer or micron length scale), transport measurements are typically performed across length scales of hundreds of microns. In this study, we present a method to relate local morphology and ionic conductivity in a block copolymer electrolyte.

Sax and Ottino developed a widely-adopted model based on effective medium theory to relate structure and transport at the bulk scale in randomly-oriented morphologies relevant to block copolymer materials.[9] Within this model, the ionic conductivity of a block copolymer electrolyte, σ, is given by

$$\sigma = f \phi_c \sigma_c \quad (1)$$

where f is the morphology factor, σ_c is the intrinsic conductivity of the bulk ion-transporting microphase phase, and ϕ_c is the volume fraction of the ion-transporting microphase.[17] Others have proposed modifications to the model in equation 1 to account for additional structural details such as tortuosity and the non-conducting interfacial volume between micrphases.[24,25] For randomly-oriented lamellae in a bulk three-dimensional material, *f* is 2/3; two out of three principle orientations lead to conduction. By similar logic, for a one-dimensional morphology in two dimensions such as a cross section through bulk lamellae, *f* is 1/2.

One of the benefits of the effective medium model is its simplicity, as it only requires knowledge of the block copolymer morphology. However, a number of recent publications have noted deviations between experiments and the ideal morphology factor predicted by effective medium theory, suggesting that defects such as grain boundaries may affect ion transport, either positively or negatively.[26–31] Majewski *et al*. compared ionic conductivities of electrolytes consisting of randomly oriented and single-grain, aligned hexagonally-packed cylinders and showed that the ratio of morphology factors $f_{Random}/f_{Aligned}$ is around 0.10 instead of 0.33, as predicted by effective medium theory.[19] Young *et al*. found that as the conductive phase becomes more networked, progressing from lamellae to hexagonally-perforated lamellae to hexagonally packed cylinders with a majority conductive phase, the morphology factor increases and becomes closer to the effective medium theory prediction.[30] Meek *et al*. provide a review of several other examples of deviations that have been observed between experiment and effective medium theory in materials based on polymerized ionic liquids.[26,27,31] These studies all suggest that defects decrease the conductivity of the block copolymer by decreasing the connectivity of the conductive phase. In contrast, Diederichsen *et al*. showed that as the number of node-like defects in a conducting network increases, the conductivity increases.[32] Similarly, in reference 33, it was shown that as *L* increases from 13 nm to 88 nm, a factor of 6.5, *f* decreases from 0.36 to 0.058, a factor of 6.2. As *L* increases, the number of grain boundary defects decreases. Improving the connection between local structure and ion transport could help clarify which defects enhance transport and which ones inhibit it.

Recently, several authors have made progress toward relating local structure and transport in thin film block copolymers. In the study by Diederichsen *et al*., block copolymers films were used to template an electronically conductive gold network. The authors use scanning electron microscopy (SEM) to characterize the local structure and directly probe the conductivity of the gold network.[32] Using this approach, the authors could relate the network topology to the electrical conductivity. In another study, Arges *et al*. use electrodes deposited on a silicon wafer

to probe the ionic conductivity of an anion-conducting thin film block copolymer based on a polymerized ionic liquid.[34] This experimental design enables the direct measurement of ionic conductivity by ac impedance spectroscopy and structure by SEM. In both of these experiments, the thin film configuration facilitates the measurement of local structure and transport on the same system.

While previous studies have shed light on the relationship between charge transport and morphology in some idealized systems, the challenge of establishing the relationship between these quantities in block copolymer electrolyte films remains. In an attempt to address this challenge, we simulate ion conduction through scanning transmission electron microscopy (STEM) images of a microtomed bulk lamellar block copolymer electrolyte for lithium metal batteries. The electrolyte consists of polystyrene-*block*-poly(ethylene oxide) (SEO) mixed with a lithium salt, lithium bis(trifluoromethanesulfonyl) imide (LiTFSI). The polystyrene (PS) block provides high modulus, and the poly(ethylene oxide) (PEO) block solvates the LiTFSI. Together, the PEO/LiTFSI mixture forms the ion-conducting phase.[35] Conductivity was simulated in two sets of images, one from an annealed sample large with grains and one from an unannealed sample with small grains. The samples used in this study are the same ones used in reference 33, where we reported on the effect of annealing on ionic conductivity. This enables a direct comparison between simulation and experiment. While our conductivity measurements are made on samples that are 100 µm thick, the STEM experiments are restricted to length scales of about 1 µm. The main question that we answer is the following: Can morphological characterization on the local scale (1 µm) can be used to predict ion transport in bulk?

EXPERIMENTAL

Materials

An SEO polymer was synthesized using sequential anionic polymerization, as described previously.[36,37] The number-average molecular weight, M_n, of the PS block is 4.9 kg mol^{-1} and that of the PEO block is 5.5 kg mol^{-1}. All steps of the electrolyte preparation were conducted in argon glovebox.[33,38] Polymer was dried under vacuum at 90 °C for 24 h, and LiTFSI was dried under vacuum at 120 °C for 72 h, both in the antechamber of an argon glovebox. The electrolyte was prepared by mixing a 10 mL solution of SEO in anhydrous benzene with a 200 µL solution of LiTFSI salt in anhydrous tetrahydrofuran and freeze drying. The sample was freeze dried without exposure to air using a homebuilt transfer apparatus and then dried under vacuum for 24 h in the antechamber of an argon glovebox. The molar ratio of Li to ethylene oxide moieties, or *r*-value was 0.085.

For both the annealed and unannealed samples, the freeze dried electrolyte was pressed into a 150 µm thick fiberglass-reinforced epoxy spacer (Garolite G10) at room temperature and vacuum-sealed in an air-tight laminated aluminum pouch (Showa-Denko). After sealing, the annealed sample was heated to 120 °C on a hotplate for 24 h, and the un-annealed sample was maintained at room temperature. The electrolyte used in this study is the same as the electrolyte used in reference 33. Immediately prior to imaging by STEM, samples were removed from their pouch. Sections of each sample, 100 nm thick, were prepared by cryo-microtoming the bulk electrolyte at -120 °C using a Leica EM FC6 microtome. The samples were placed on lacey carbon-coated copper grids and stained with RuO4 vapor for 10 min. The electrolytes were imaged with a Tecnai F20 UT FEG instrument using a high angle annular dark field detector, with the PEO domains appearing bright.[39] The acceleration voltage was 200 keV.

Simulation Domain Preparation

STEM images were converted to binary, black and white images for simulations. Small variations in magnification of the 8-bit grayscale STEM images were eliminated by cropping the

images to a consistent physical size (0.985 x 0.985 µm) and compressing them to a consistent resolution (1024 x 1024 pixels). To eliminate noise and long-range intensity fluctuations due to variations in sample thickness, a bandpass filter was applied using the ImageJ software package. The lower cutoff was set to 4 pixels and the upper cutoff set to 20 pixels. The images were segmented to produce binary images. The segmentation threshold was adjusted so that the area fraction of the conducting phase (represented as white), ϕ, was as close as possible to the volume fraction of the conducting phase in the bulk electrolyte, ϕ_c, 0.58. Circular regions were extracted from segmented microscopy image data using a custom ImageJ script, and a commercial software package (Avizo, FEI) was used to convert the circular regions into surface meshes.

Modeling

The surface meshes were imported into a commercial simulation package (STAR-CCM+, CD-adapco) and transformed into surface meshes in annular regions, with the inner and outer edges of these regions virtually embedded into circular electrodes of small but finite width. These regions were refined with a custom mesh repair algorithm, and transformed into simulation domains, on which the Laplace equation with potential boundary conditions was then solved. Conductivity ratios were computed from the simulation results. Different boundary conditions and image regions could be used for the simulations. For example, a square image region could be used with potential boundary conditions on two parallel sides and insulating boundary conditions on the other two sides. In this configuration, some paths through the electrolyte would terminate on the insulating boundaries, rendering them non-conducting. Annular image regions with circular electrodes were chosen for this study in order to maximize the number of conductive paths between electrodes and to avoid directional bias in the plane. In Figure S1, electric potential distribution is shown for the image Annealed 2 in both annular and square geometry.

The conductivity ratio is a characteristic of the material. However, in order to obtain these values through simulation, selected spatial domains must be representative of the material. They must be sufficiently large to make the effect of local variation unimportant; in this work, the outer diameters of the annular regions were taken as the image widths. Also, an inner electrode that is too small will be connected to rest of the spatial domain by only a small number of conductive paths, producing a spatial domain that is not representative of the segmented image data. For each segmented image, a suitable inner electrode size was chosen by constructing several domains from the image, each using a different inner radius. As discussed, the conductivity ratios tend to vary with inner electrode size when the inner electrodes are small, as well as when the inner electrodes are too large, making the area of the domain too small. However, the conductivity ratios tend to reach a plateau at intermediate sizes of the inner electrode. The values reported in this article are based on these intermediate sizes, for which variation of effective conductivity with electrode size is within approximately 5 %. The effect of inner radius on effective conductivity is reported in Figure S2 in the supporting information.

Direct numerical simulations were performed on planar spatial domains constructed from microscopy images. In the annular region used, the inner and outer boundaries represent electrodes held at different potentials. As a baseline, the potential of an annular region consisting entirely of conductive material is given by Laplace's equation (equation 2).

$$\nabla^2 V = 0 \qquad (2)$$

The potential is held at 1 V at the inner boundary at radius $R_i$and at 0 V at the outer boundary at radius R_o. The potential as a function of radial position *r* is then given by equation 3.

$$V(r) = \frac{\ln(r/R_o)}{\ln(R_i/R_o)} \quad (3)$$

Though a dc potential is applied to the electrolyte, polarization effects are ignored.[40] This treatment is representative of conditions during a low-amplitude ac impedance experiment.

The total current flowing between the two electrodes may be determined from the current density at some radial position and the circumference of the circle associated with that position, but is independent of radial position. The current density $\boldsymbol{j}$ can be obtained from the potential as $\boldsymbol{j} = \sigma_c \boldsymbol{E}$, where σ_c is the bulk conductivity of the conductive material and $\boldsymbol{E} = \nabla V$ is the electric field. The total current per unit depth (assuming no variation of the spatial domain out of the plane) is then given by equation 4.

$$I_{\text{analytical}} = 2\pi r|\boldsymbol{j}(r)\cdot\hat{\boldsymbol{r}}| = 2\pi r\sigma_c\left|\frac{dV}{dr}\right|$$

$$= \frac{2\pi\sigma_c}{|\ln(R_i/R_o)|} \quad (4)$$

This analytical result may be compared against the current per unit depth computed in simulations involving similar spatial domains based on microscopy images. Unlike in the baseline case, these spatial domains consist of complex arrangements of both conductive and insulating regions. However, the total current passing between the electrodes can be computed through any surface represented by a closed, non-intersecting curve encircling the inner electrode in the simulation domain. Based on the computed current, one can assign a conductivity, σ, to the simulation domain through the analytical relationship obtained earlier (equation 5).

$$I_{\text{sim}} = \frac{2\pi\sigma}{|\ln(R_i/R_o)|} \quad (5)$$

Rearranging this expression and reintroducing the bulk conductivity of the conductive material gives equation 6, which is a conductivity ratio that reflects only the arrangement of conductive and insulating regions in the image data.

$$\frac{\sigma}{\sigma_c} = \frac{I_{\text{sim}}}{\sigma_c}\frac{|\ln(R_i/R_o)|}{2\pi} \quad (6)$$

This conductivity ratio is related to *f*, where ϕ is the area fraction of the conductive phase in the image, or ϕ_c, the conductive phase volume fraction in a bulk sample (equation 7).

$$f = \frac{\sigma}{\sigma_c\phi} \quad (7)$$

RESULTS

In Table 1, the properties of the annealed and unannealed samples at the bulk and local scale are summarized. The bulk properties, average grain size, L_{SAXS}, and domain spacing, d_{SAXS}, measured by small angle X-ray scattering (SAXS), are taken from reference 33. The bulk volume fraction of the conductive PEO/LiTFSI domain, ϕ_c, is estimated to be 0.58 based on a rule of mixtures (equation 8).

$$\phi_c = \frac{v_{EO} + r\,v_{LiTFSI}}{v_{EO} + r\,v_{LiTFSI} + \frac{n_{PS}}{n_{PEO}}v_S} \quad (8)$$

In equation 8, v_{EO} is the molar volume of the ethylene oxide monomer, calculated from the molar mass of 44.05 g mol^{-1} and bulk PEO density, 1.12 g cm^{-3}, v_S is the molar volume of the styrene monomer, calculated from the molar mass of 104.15 g mol^{-1} and bulk PS density of 1.07 g cm^{-3}, v_{LiTFSI} is the molar volume of the salt, calculated from the molar mass of 287.09 g mol^{-1} and bulk density of 2.02 g cm^{-3}, n_{PEO} is the number of monomers in the PEO block, and n_{PS} is the number of monomers in the PS block.[41]

Binarized STEM images were analyzed to obtain the local properties reported in Table 1: conductive phase areas fraction, ϕ, local grain size, L_{TEM}, local domain spacing, d_{TEM}, anisotropy factor, *a*, electric potential standard deviation at a radius of 286 nm, $S_{V(286)}$, and morphology factor, *f*. In Figure 1, a series of images illustrating the image processing steps are shown for an annealed sample (Figure 1a-c), and

TABLE 1 Bulk and local properties. Bulk properties are taken from reference 33. The bulk properties conductive phase volume fraction, ϕ_c, grain size measured by SAXS, L_{SAXS}, and domain spacing measured by SAXS, d_{SAXS}, are reported along with the local properties, conductive phase area fraction, ϕ, grain size measured by STEM, L_{TEM}, domain spacing measured by STEM, d_{TEM}, alignment parameter, a, electric potential standard deviation at mid-radius, $S_{V(286)}$, and morphology factor, f.

	Bulk Properties			Local Properties					
	ϕ_c	L_{SAXS} (nm)	d_{SAXS} (nm)	ϕ	L_{TEM} (nm)	d_{TEM} (nm)	a	$S_{V(286)}$ (V)	f
Annealed 1				0.59	88	14.2	0.49	0.13	0.46
Annealed 2				0.59	85	16.7	0.51	0.24	0.48
Annealed 3				0.58	48	17.0	0.50	0.14	0.40
Annealed 4				0.58	42	16.0	0.50	0.13	0.50
Average	0.58	88	16.8		65 ± 22	16.0 ± 0.2		0.16 ± 0.05	0.45 ± 0.04
Unannealed 1				0.58	10.9	16.3	0.50	0.08	0.39
Unannealed 2				0.58	11.6	16.3	0.51	0.14	0.39
Unannealed 3				0.59	11.9	16.2	0.50	0.12	0.36
Unannealed 4				0.58	11.7	15.9	0.44	0.06	0.33
Average	0.58	13	16.0		11.5 ± 0.4	16.2 ± 1.1		0.10 ± 0.03	0.37 ± 0.03

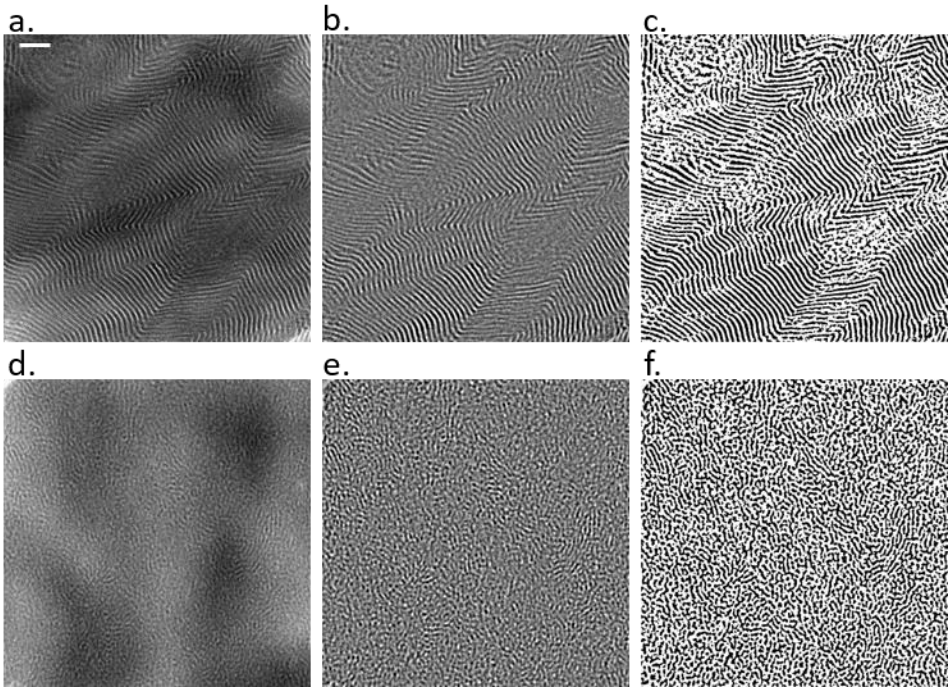

FIGURE 1 Raw and processed images of an annealed sample, Annealed 2, (a)-(c), and an unannealed sample, Unannealed 1, (d)-(f). The scale bar in (a) represents 100 nm and applies to all of the images. Images (a) and (d) show the raw, RuO_4-stained STEM images, (b) and (e) show the images after applying a bandpass filter, and (c) and (f) show the images after binarization. The light domains represent the conductive phase.

an unannealed sample (Figure 1d-f). The annealed images correspond to Annealed 2 in Table 1, and the unannealed images correspond to Unannealed 1. Figures 1a and 1d show the raw stained STEM images, Figures 1b and 1e show the images after applying a bandpass filter, and Figures 1c and 1f show images after binarization. Images such as Figures 1c and 1f were converted to circular surface meshes and used as inputs to the conductivity simulation. The light domains in the images represent the conductive phase. The area fraction of the conducting phase in each image, ϕ, is reported in Table 1. The values for ϕ are very close to those of ϕ_c due to the approach used in the analysis (see Simulation Domain Preparation) but they are not identical. During the binarization of images, small variations occur in ϕ due to the discrete nature of the raw 8-bit grayscale STEM images.

Local grain size, L_{TEM}, and domain spacing, d_{TEM} were computed using an open-source macro for the ImageJ software program, ADAblock, written by Murphy *et al*.[42] Figures 2a and 2b show false-color orientation maps produced using the ADAblock program, with color representing the orientation of the lamellar domains. In Figure 2, black regions represent conducting domains. The values for L_{TEM} were determined for each image by using the orientation map to calculate the orientational correlation length at a subset of 4000 points in the image, and averaging. The orientational correlation length is taken to be the grain size, L_{TEM}. Values for L_{TEM} reported in Table 1 represent the average of results from three different sets of 4000 points, and the standard deviations between measurements were all within 7 %. The values of L_{SAXS} and L_{TEM} are in reasonable agreement for both the annealed and unannealed samples: 65 ± 22 nm (TEM) and 88 nm (SAXS) for the annealed sample, and 11.5 ± 0.4 nm (TEM) and 13 nm (SAXS) for the unannealed sample. The values of d_{SAXS} and d_{TEM} are also in good agreement for both the annealed and unannealed samples: 16.0 ± 0.2 nm (TEM) and 16.8 nm (SAXS) for the annealed sample, and 16.2 ± 1.1 nm (TEM) and 16.0 (SAXS) for the unannealed sample. The values of grain size and domain spacing measured by TEM are close to the values measured by SAXS, indicating that the regions of electrolyte in the images are representative of the bulk electrolytes.

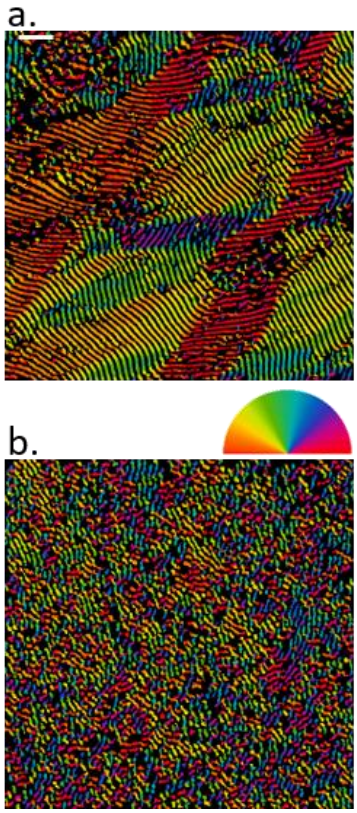

FIGURE 2 Orientation maps based on STEM images of an annealed sample, Annealed 2, (a) and an unannealed sample, Unannealed 1, (b). The scale bar represents 100 nm. Black regions are conducting domains. The color scale indicates orientation angle. Images and color scale were produced using the ADAblock program for ImageJ.[42]

An assumption of effective medium theory is that grains are randomly oriented. To check if grain orientation was random on the length scale of the images, an alignment parameter, a, was calculated for the images according to equation 9.[43]

$$a = \langle \cos^2\{ \theta_{\mathrm{Domain}}(x,y) - \theta(x,y) \} \rangle \quad (9)$$

In equation 9, θ_{Domain} is the orientation angle of the domain tangent, and θ is the azimuthal angle at a given point (x, y) in the image. The data for $\theta_{\mathrm{Domain}}(x, y)$ is obtained from the color scale in domain orientation maps such as those in Figure 2. The alignment parameter is calculated by averaging the correlation between θ_{Domain} and θ over all points in the conductive regions of the annular simulation domain. Both angles are restricted to vary between 0 and 180°, and *a* varies between 0 and 1, where the value 0.5 indicates random grain orientation and 1 indicates grain alignment along the radial, conductive direction. For all but one image, the values of *a* are very close to 0.5, indicating that the assumption that grains are randomly oriented is valid for the simulation domains. For the image Unannealed 4, *a* is 0.44, below 0.5, indicating that the grains are preferentially aligned in the direction perpendicular to conduction.

The local properties $S_{\mathrm{V}(286)}$ and f were determined from the simulated electric potential. In Figure 3, representative electric potential maps are shown for an annealed sample (Figure 3a) and an unannealed sample (Figure 3b). The simulation results shown in Figure 3 are based on the images in Figure 1c and 1f. In Figure 3a, the change in potential with radius is anisotropic. Regions where the lamellae are aligned in the radial direction appear to be different from regions where the lamellae are aligned in the azimuthal direction. Not all conductive paths between the inner and outer electrodes are equivalent. In Figure 3b, the change in potential with radius appears to be more isotropic indicating that the conductive paths are networked and roughly equivalent through the image.

The difference in potential distribution between annealed and unannealed samples is illustrated in Figure 4. In Figure 4a, the azimuthally-averaged potential, $V_{\mathrm{Ave}}(r)$, is averaged over the four images and plotted as a function of radius, *r*. The error bars represent the standard deviation of the average over four images. The analytic solution for the potential distribution in a homogenous conducting phase (equation 4) is included for comparison. The potential distributions for both annealed and unannealed samples are similar to the analytic solution. In Figure 4b, the standard deviation of the azimuthally-averaged potential, S_{V}, (magnitude of error bars in Figure 4a) is plotted as a function of radius. Each point shown in Figure 4b is averaged over four images. Because the potential at the inner and outer radii, R_i (121 nm) and R_o (493 nm), are fixed, the standard deviations at the boundaries are nearly zero for all samples; the standard deviations are not exactly zero due to numerical error in the image analysis. The value of S_{V} at radii between R_i and R_o gives a measure of the anisotropy of the images, with higher S_{V} indicating greater anisotropy. In Table 1, values of S_{V} at the mid-radius of 286 nm, $S_{\mathrm{V}(286)}$, are reported. On average the images from the annealed sample have higher values of $S_{\mathrm{V}(286)}$ than images from the unannealed sample (0.16 ± 0.05 V vs 0.10 ±

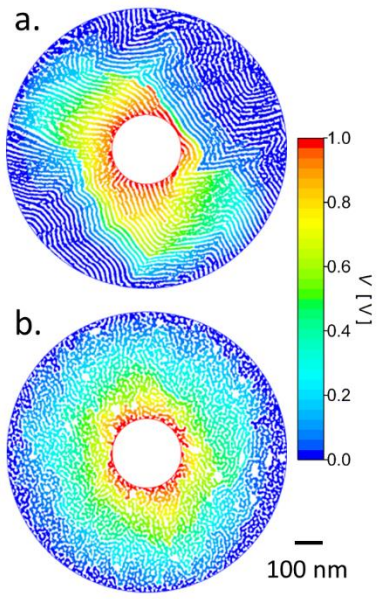

FIGURE 3 Simulated electric potential maps for an annealed sample, Annealed 2, (a) and an unannealed sample, Unannealed 1, (b). The color scale indicates the electric potential, *V*, and white regions are non-conducting. The scale bar is indicated in the bottom right.

0.03 V). However, given that the value of L_{TEM}, is approximately four to eight times higher for the images from the annealed sample, the difference in $S_{V(286)}$ is small by comparison. It is perhaps surprising that L_{TEM} and $S_{V(286)}$ do not appear to be strongly linked. One explanation could be that $S_{V(286)}$ is more sensitive to local grain size at a radius of 286 nm than the image-average grain size, L_{TEM}.

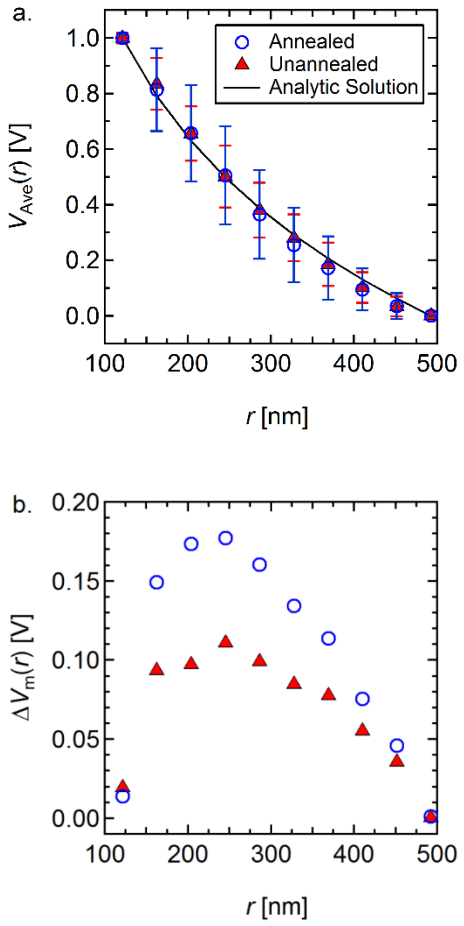

FIGURE 4 Azimuthally-averaged electric potential, $V_{Ave}(r)$ (a), and standard deviations of electric potential S_V averaged among images from annealed and unannealed samples, (b). In (a) the analytic solution for a homogenous conductor in an annular geometry, equation 4, is also plotted.

Morphology factor, f, was calculated based on the simulated current, I_{Sim}, (equations 5-7). The values of f for the annealed samples are between 0.40 and 0.50 with an average of 0.46 ± 0.04, and the values of f for the unannealed samples are between 0.33 and 0.39 with an average of 0.37 ± 0.03. Though on average the annealed images have a higher value of f, according to Table 1, f is not strongly correlated with L_{TEM} or $S_{V(286)}$ on the level of individual images. For example, in the set of annealed images, the values of $S_{V(286)}$ and L_{TEM} are similar for Annealed 3 and Annealed 4, but Annealed 3 has the lowest value of f at 0.40 and Annealed 4 has the highest at 0.50. The ideal value of f in two dimensions is 0.5. This prediction is remarkably consistent with the morphology factors calculated for the annealed samples but higher than the morphology factors calculated for the unannealed samples. For the image Unannealed 4, the low value of f corresponds to a low value of a, however, for the other images from the unannealed sample, the reason for the low value of f is not known. Given the variation in f from sample to sample, the primary conclusions of the analysis of the STEM micrographs are that f is a weak function of grain size and that annealing results in a slight increase in f. The ratio $f_{Unannealed}/f_{Annealed}$ obtained by using the average values of the two quantities is 0.82.

The main objective of this study is to compare the local ion transport characteristics determined by simulation with macroscopic measurement of bulk conductivity. There are two main differences between the two approaches:
(1) The local transport characteristics were determined in 2D simulations while the bulk measurements were obtained in 3D samples.
(2) The local characteristics were determined from analysis of a very small subset of the grains that were sampled in the bulk measurements.

The ratio $f_{Unannealed}/f_{Annealed}$ does not depend on the dimension of the system. We can thus use this ratio to account for difference (1) above. The simulated and experimental values of $f_{Unannealed}/f_{Annealed}$ are reported in Table 2. It is clear that the local analysis provides no explanation for the observation that in bulk

measurements, $f_{Unannealed}/f_{Annealed}$ in this sample is 6.2. The discrepancy in Table 2 suggests that accurate determination of bulk transport requires determination of nanoscale morphology over a significantly larger region than that employed in the present study (approximately 1 μm).

TABLE 2 Morphology factor ratio from simulation and experiment. The experimental result is taken from reference 33.

	$f_{Unannealed}/f_{Annealed}$
Simulation	0.82
Experiment	6.2

Finally, we note that in our simulation, the intrinsic conductivity of the PEO/LiTFSI phase is assumed to be constant. If annealing induces any changes in intrinsic conductivity, such effects would not be captured by the simulation. Annealing could change the intrinsic conductivity of the PEO/LiTFSI phase in two ways:
(1) The interfacial mixing between the non-conducting and conducting phase could change with annealing.
(2) The intrinsic conductivity at grain boundaries could be different from that in the interior of a lamellar grain.

As the electrolyte is annealed from a less ordered, freeze-dried state to a more ordered state, we expect the intermixing to either decrease or stay constant. This should result in an increase in conductivity upon annealing; however, the opposite is observed in experiment. Hence, it is unlikely that the first factor can account for the discrepancy between simulation and experiment.

It is possible that non-equilibrium structures such as grain boundaries have different intrinsic conductivities from the interior of a grain. The experimental morphology factor ratio and discrepancy between simulation and experiment could be explained if conductivity is higher at grain boundaries than in the interior of a grain. To date, most characterization of SEO/LiTFSI electrolytes has been performed on annealed samples.[38,44] Further experimental work is needed to determine if segmental dynamics and intrinsic conductivity differ in grain boundaries.

CONCLUSIONS

We have presented a method to relate local morphology to ionic conductivity in a block copolymer electrolyte based on simulating the electric potential distribution through 2D binarized STEM images of a sectioned bulk electrolyte. Two samples were imaged, an annealed electrolyte with large grain size and an unannealed electrolyte with small grain size. A morphology factor, f, was calculated based on the simulated electric potential distributions. The average value of f for images from annealed samples is 0.45 ± 0.04, and the average value of f for images from the unannealed samples is 0.37 ± 0.03. The value of f for both sets of samples is surprisingly close to the ideal value predicted by effective medium theory, 0.5. The fact that ion transport through grains in regions with length scales in the vicinity of 1 μm can be described by effective medium theory is an important conclusion of the present study.

However, the main objective of this study was to provide insight into the experimentally observed effect of annealing block copolymer electrolytes on bulk conductivity. The present simulations provide no basis for the experimental observations; in simulations, the ratio $f_{Unannealed}/f_{Annealed}$ is 0.82, and in experiments, it is 6.2. Further work is needed to understand the origin of this discrepancy. One possibility is that local ion transport is fundamentally different in 2D and 3D and thus one needs to image and simulate 3D morphologies. While considerable work will be required to examine this possibility, it can readily be done as 3D morphology can be determined by electron tomography.[45,46] However, given the fact that our 2D results were in good agreement with effective medium theory, it is unlikely that the 3D results will differ significantly from that theory. It is more likely

that annealing results in changes in the conducting pathways that are entirely not captured in the images that we have obtained thus far. For example, it is important to note that a single T-junction defect oriented perpendicular to the direction of ion transport located at any point along the conduction pathway will block ion transport along that pathway. It appears that understanding the relationship between local and bulk ion transport in randomly oriented block copolymer grains requires accurate determination of morphology over length scales much larger than 1 μm. These experiments will be considerably more challenging using conventional, well-developed tools used for block copolymer morphology characterization such as TEM, STEM, and SAXS. A third possible explanation for the discrepancy between theory and experiment is that the simulations do not capture changes in intrinsic conductivity that might occur with annealing. Further experimental work is needed to characterize segmental dynamics at grain boundaries in block copolymer electrolytes.

ACKNOWLEDGEMENTS

This work was supported by the Assistant Secretary for Energy Efficiency and Renewable Energy, Office of Vehicle Technologies of the US Department of Energy under Contract DE-AC02-05CH11231 under the Battery Materials Research program. The STEM work performed by X.C. Chen was supported by the Electron Microscopy of Soft Matter Program from the Office of Basic Energy Sciences of the U.S. Department of Energy under Contract No. DE-AC02-05CH11231. The authors gratefully acknowledge CD-adapco support engineer Megan Karalus for her advice in using STAR-CCM+ to perform the simulations in this work.

REFERENCES AND NOTES

1. J. R. Varcoe, R. C. T. Slade, *Fuel Cells* **2005**, *5*, 187–200.
2. Y. A. Elabd, M. A. Hickner, *Macromolecules* **2011**, *44*, 1–11.
3. M. Tanaka, K. Fukasawa, E. Nishino, S. Yamaguchi, K. Yamada, H. Tanaka, B. Bae, K. Miyatake, M. Watanabe, *J. Am. Chem. Soc.* **2011**, *133*, 10646–10654.
4. Y. Yang, S. Holdcroft, *Fuel Cells* **2005**, *5*, 171–186.
5. H.-S. Lee, A. S. Badami, A. Roy, J. E. McGrath, *J. Polym. Sci. Part Polym. Chem.* **2007**, *45*, 4879–4890.
6. B. Bae, K. Miyatake, M. Watanabe, *ACS Appl. Mater. Interfaces* **2009**, *1*, 1279–1286.
7. A. E. Ozcam, N. Petzetakis, S. Silverman, A. K. Jha, N. P. Balsara, *Macromolecules* **2013**, *46*, 9652–9658.
8. D. J. Kinning, E. L. Thomas, *Macromolecules* **1987**, *20*, 1129–1133.
9. J. Sax, J. M. Ottino, *Polym. Eng. Sci.* **1983**, *23*, 165–176.
10. G. E. Sanoja, B. C. Popere, B. S. Beckingham, C. M. Evans, N. A. Lynd, R. A. Segalman, *Macromolecules* **2016**, *49*, 2216–2223.
11. E. A. Jackson, M. A. Hillmyer, *ACS Nano* **2010**, *4*, 3548–3553.
12. W. A. Phillip, B. O'Neill, M. Rodwogin, M. A. Hillmyer, E. L. Cussler, *ACS Appl. Mater. Interfaces* **2010**, *2*, 847–853.
13. F. A. Digiano, A. Roudman, M. Arnold, B. Freeman, *Environ. Eng. Sci.* **2002**, *19*, 497–511.
14. V. I. Bondar, B. D. Freeman, I. Pinnau, *J. Polym. Sci. Part B Polym. Phys.* **2000**, *38*, 2051–2062.
15. A. Car, C. Stropnik, W. Yave, K. V. Peinemann, *J. Membr. Sci.* **2008**, *307*, 88–95.
16. W. S. Young, W. F. Kuan, T. H. Epps, *J. Polym. Sci. Part B Polym. Phys.* **2014**, *52*, 1–16.
17. M. Singh, O. Odusanya, G. M. Wilmes, H. B. Eitouni, E. D. Gomez, A. J. Patel, V. L. Chen, M. J. Park, P. Fragouli, H. Iatrou, N. Hadjichristidis, D. Cookson, N. P. Balsara, *Macromolecules* **2007**, *40*, 4578–4585.
18. Y. Gu, S. Zhang, L. Martinetti, K. H. Lee, L. D. McIntosh, C. D. Frisbie, T. P. Lodge, *J. Am. Chem. Soc.* **2013**, *135*, 9652–5.

19. P. W. Majewski, M. Gopinadhan, W. Jang, J. L. Lutkenhaus, C. O. Osuji, *J. Am. Chem. Soc.* **2010**, *132*, 17516–17522.
20. I. Gunkel, T. Thurn-Albrecht, *Macromolecules* **2012**, *45*, 283–291.
21. C. M. Bates, A. B. Chang, N. Momčilović, S. C. Jones, R. H. Grubbs, *Macromolecules* **2015**, *48*, 4967–4973.
22. L. D. McIntosh, M. W. Schulze, M. T. Irwin, M. A. Hillmyer, T. P. Lodge, *Macromolecules* **2015**, *48*, 1418–1428.
23. A.-V. G. Ruzette, P. P. Soo, D. R. Sadoway, A. M. Mayes, *J. Electrochem. Soc.* **2001**, *148*, A537–A543.
24. R. Bouchet, T. N. T. Phan, E. Beaudoin, D. Devaux, P. Davidson, D. Bertin, R. Denoyel, *Macromolecules* **2014**, *47*, 2659–2665.
25. V. Ganesan, V. Pyramitsyn, C. Bertoni, M. Shah, *ACS Macro Lett.* **2012**, *1*, 513–518.
26. R. L. Weber, Y. Ye, A. L. Schmitt, S. M. Banik, Y. A. Elabd, M. K. Mahanthappa, *Macromolecules* **2011**, *44*, 5727–5735.
27. K. M. Meek, S. Sharick, Y. Ye, K. I. Winey, Y. A. Elabd, *Macromolecules* **2015**, *48*, 4850–4862.
28. Y. A. Elabd, E. Napadensky, C. W. Walker, K. I. Winey, *Macromolecules* **2006**, *39*, 399–407.
29. M. Umeda, I. Uchida, *Langmuir* **2006**, *22*, 4476–4479.
30. W. S. Young, T. H. Epps, *Macromolecules* **2012**, *45*, 4689–4697.
31. J. H. Choi, Y. Ye, Y. A. Elabd, K. I. Winey, *Macromolecules* **2013**, *46*, 5290–5300.
32. K. M. Diederichsen, R. R. Brow, M. P. Stoykovich, *ACS Nano* **2015**, *9*, 2465–2476.
33. M. Chintapalli, X. C. Chen, J. L. Thelen, A. A. Teran, X. Wang, B. A. Garetz, N. P. Balsara, *Macromolecules* **2014**, *47*, 5424–5431.
34. C. G. Arges, Y. Kambe, H. S. Suh, L. E. Ocola, P. F. Nealey, *Chem. Mater.* **2016**, *28*, 1377–1389.
35. E. D. Gomez, A. Panday, E. H. Feng, V. Chen, G. M. Stone, A. M. Minor, C. Kisielowski, K. H. Downing, O. Borodin, G. D. Smith, N. P. Balsara, *Nano Lett.* **2009**, *9*, 1212–6.
36. R. P. Quirk, J. Kim, C. Kausch, M. Chun, *Polym. Int.* **1996**, *39*, 3–10.
37. N. Hadjichristidis, H. Iatrou, S. Pispas, M. Pitsikalis, *J. Polym. Sci. Part Polym. Chem.* **2000**, *38*, 3211–3234.
38. R. Yuan, A. A. Teran, I. Gurevitch, S. A. Mullin, N. S. Wanakule, N. P. Balsara, *Macromolecules* **2013**, *46*, 914–921.
39. F. I. Allen, P. Ercius, M. A. Modestino, R. A. Segalman, N. P. Balsara, A. M. Minor, *Micron Oxf. Engl. 1993* **2013**, *44*, 442–50.
40. J. Newman, K. Thomas-Alyea, *Electrochemical Systems*, Wiley-Interscience, Hoboken, **2004**.
41. R. A. Orwoll, in *Phys. Prop. Polym. Handb.* (Ed.: J.E. Mark), Springer, New York, **2007**, pp. 94–95.
42. J. N. Murphy, K. D. Harris, J. M. Buriak, *PLoS ONE* **2015**, *10*, 1–32.
43. R. J. Roe, *Methods of X-Ray and Neutron Scattering in Polymer Science*, Oxford University Press, New York, NY, **2000**.
44. M. Chintapalli, T. N. P. Le, N. R. Venkatesan, N. G. Mackay, A. A. Rojas, J. L. Thelen, X. C. Chen, D. Devaux, N. P. Balsara, *Macromolecules* **2016**, *49*, 1770–1780.
45. H. Jinnai, T. Tsuchiya, S. Motoki, T. Kaneko, T. Higuchi, A. Takahara, *J. Electron Microsc. (Tokyo)* **2013**, *62*, 243–258.
46. V. H. Mareau, S. Akasaka, T. Osaka, H. Hasegawa, *Macromolecules* **2007**, *40*, 9032–9039.

GRAPHICAL ABSTRACT

AUTHOR NAMES

Mahati Chintapalli, Kenneth Higa, X. Chelsea Chen, Venkat Srinivasan, Nitash P. Balsara

TITLE

Simulation of local ion transport in lamellar block copolymer electrolytes based on electron micrographs

TEXT

Relating local structure and long-range transport properties is a challenge in nanostructured polymers. Local ionic conductivity is estimated by combining simulations and transmission electron micrographs of lamellar block copolymer electrolytes for lithium batteries. On the length scale of the micrographs (1 µm), simulations agree with predictions based on effective medium theory, but deviate from experimental values measured across macroscopic samples (100 µm).

GRAPHICAL ABSTRACT FIGURE